Ge et al. Cell Communication and Signaling (2026) 24:159
https://doi.org/10.1186/s12964-026-02689-3

Cell Communication and Signaling

RESEARCH Open Access

RT–ICI therapy induces a distal immunometabolic axis that shapes systemic macrophage polarization and enhances local T cell immunity

Yizhi Ge[1†], Haitao Liu[2†], Jiayi Shen[3], Hongming Xu[4], Yong Feng[1*], Dan Zong[1*] and Lijun Wang[1*]

Abstract

Colorectal cancer (CRC) liver metastases remain refractory to immunotherapy due to a profoundly immunosuppressive tumor microenvironment. Here, we conducted a prospective clinical study enrolling 18 patients with microsatellite-stable CRC liver metastases treated with high-dose radiotherapy (RT) followed by anti–PD-1 immune checkpoint inhibitors (RT–ICI). Integrative analysis of single-cell RNA-sequencing, spatial transcriptomics, and peripheral immune profiling revealed that RT–ICI therapy reprograms both tumor-intrinsic and immune compartments. RT triggered the emergence of an APOA2$^+$ tumor cell state characterized by enhanced lipid metabolic activity and transient elevation of circulating HDL. This metabolic reprogramming, in turn, promoted systemic activation of CETP$^+$ M2-like macrophages, a population marked by high LXR/RXR transcriptional activity and enriched expression of immunosuppressive and lipid-processing genes. Despite their expansion, CETP$^+$ macrophages localized preferentially to non-irradiated tumor regions, suggesting a distal immunometabolic effect driven by HDL-mediated signaling. Concurrently, combination therapy expanded GZMB$^+$ effector T cells and induced a novel population of inflammatory–toxic T cells (IT_T), which exhibited high cytotoxicity and spatial co-localization with CXCL10$^+$ macrophages. Ligand–receptor analysis and pseudotime modeling revealed that irradiated tumor cells acted as "in situ vaccines" by enhancing MHC–TCR interactions and promoting T cell differentiation along non-exhausted cytotoxic lineages. Together, these findings reveal a dual mechanism by which RT–ICI therapy enhances local anti-tumor immunity while modulating systemic lipid metabolism and macrophage polarization, offering insights for combinatorial immunotherapy design in immunologically "cold" tumors.

Keywords Single-Cell sequence, Spatial transcriptomic, Colorectal cancer, Liver metastasis, High-dose radiotherapy, Tumor environment

†Yizhi Ge and Haitao Liu contributed equally to this work.

*Correspondence:
Yong Feng
fengyong@jszlyy.com.cn
Dan Zong
zongdan910@sina.com
Lijun Wang
dr_wanglj@163.com

[1]Department of Radiation Oncology, Jiangsu Cancer Hospital, Jiangsu Institute of Cancer Research, The Affiliated Cancer Hospital of Nanjing Medical University, 42 Baiziting Road, Xuanwu District, Nanjing, Jiangsu 210009, China
[2]School of Life Sciences, Fudan University, Shanghai 200438, China
[3]Jiangsu Cancer Hospital, The Affiliated Cancer Hospital of Nanjing Medical University, Jiangsu Institute of Cancer Research, Nanjing, China
[4]Department of Oncology, Huai'an 82 Hospital, Huai'an, China

Introduction

Colorectal cancer (CRC) remains one of the most common and deadly malignancies worldwide [1], with liver metastasis being the predominant cause of cancer-related mortality [2]. Although immune checkpoint inhibitors (ICIs), particularly PD-1 blockade, have demonstrated durable clinical benefit in CRC [3], the vast majority of patients with microsatellite-stable (MSS) CRC—including those with liver metastases—exhibit minimal response to PD-1 or PD-L1 inhibitors [4]. This poor efficacy has been attributed to an immunosuppressive liver microenvironment characterized by T cell exclusion, abundant tumor-associated macrophages, and impaired antigen presentation [5].

Radiotherapy (RT) has emerged as a potent immunomodulatory modality capable of converting "cold" tumors into "hot" immune-reactive lesions [6]. Recent work in lung cancer suggests RT–ICI induces CXCL16–CXCR6 recruitment of CXCL13$^+$ CD8 T cells [7]. Beyond its cytotoxic effects, RT enhances tumor immunogenicity by inducing the release of tumor-associated antigens (TAAs), upregulating MHC class I molecules, and facilitating dendritic cell maturation and T cell priming [8]. These effects provide a strong rationale for combining RT with ICIs to sensitize otherwise resistant MSS CRC to immunotherapy. Indeed, preclinical studies and early-phase clinical trials suggest that RT–ICI combination therapy can elicit systemic immune responses and overcome resistance in selected MSS CRC patients [9].

Recent evidence has underscored the importance of lipid metabolism in shaping immune responses within the tumor microenvironment [10]. Lipid accumulation can impair cytotoxic T cell function [11], promote regulatory phenotypes in macrophages, and establish immunosuppressive niches [12]. Among lipid regulators, high-density lipoprotein (HDL) and its sensor, liver X receptor alpha (LXRα), play central roles in maintaining lipid homeostasis [13] and modulating innate immune signaling [14]. LXRα forms a functional heterodimer with retinoid X receptor alpha (RXRA) [15], which binds to LXR response elements in genes governing cholesterol efflux, lipid metabolism, and macrophage polarization—such as CETP [16] and CD5L [17]. However, whether therapy-induced alterations in tumor lipid metabolism feedback to immune cells via HDL–LXR signaling has not been thoroughly explored.

In this study, we investigated the systemic and local consequences of RT–ICI combination therapy in MSS CRC patients with liver metastases using single-cell and spatial transcriptomics, lipid profiling, and immune phenotyping. We discovered that RT–ICI treatment induced a tumor subpopulation with elevated APOA2 expression, driving increased HDL biosynthesis and a transient rise in circulating HDL. This HDL surge activated the LXR–RXRA pathway in CETP$^+$ macrophages at distant sites, promoting M2-like immunosuppressive polarization—an effect we term a "distal immunometabolic response." Concurrently, RT–ICI enhanced intratumoral cytotoxicity by expanding pro-inflammatory CD8$^+$ T cell subsets, which co-localized with chemokine-producing macrophages. These findings reveal a dual mechanism of RT–ICI action—local immune activation and systemic metabolic reprogramming—and identify the HDL–LXR–CETP axis as a key player in shaping therapeutic responses.

Results

RT–ICI combination prolongs survival and suppresses tumor progression in patients with CRC liver metastases

This study enrolled 18 patients with liver metastases arising from microsatellite-stable (MSS) colorectal cancer who received combination therapy consisting of radiotherapy (RT) and PD-1 immune checkpoint inhibitors (ICIs). Patients underwent high-dose RT targeting 1 to 4 tumor lesions, administered in 3–5 fractions at a dose of 8 Gy per fraction, guided by individual clinical assessment. Within one week following completion of RT, patients initiated PD-1 blockade therapy (240 mg, intravenous infusion, every 3 weeks) and continued treatment until disease progression or study termination (Fig. 1A).

Tumor burden was assessed by CT imaging at baseline and post-treatment. Lesions located within the high-dose RT field exhibited substantial regression, with all measurable lesions decreasing in size by more than 50% (Fig. 1B-C). Flow cytometric analysis of peripheral blood revealed significant post-treatment immunological changes, characterized by a decrease in the proportion of lymphocytes and a concurrent increase in neutrophils; conversely, proportions of monocytes, eosinophils, and basophils remained relatively stable (Fig. 1D-H). Collectively, these findings suggest that RT-ICI therapy modulates systemic immune cell composition, which may contribute to enhanced anti-tumor responses.

RT–ICI combination therapy enhances lipid metabolism in tumor cells

To elucidate the remodeling of the tumor microenvironment by RT–ICI therapy, we performed single-cell RNA sequencing on paired pre- and post-treatment tumor samples. Unsupervised clustering defined nine major cell lineages (Fig. 1I, Fig. S1A-B), with re-clustering of epithelial cells identifying seven distinct subpopulations (Fig. 1J-L). Comparative analysis revealed no significant changes in chromosomal copy number variations (CNVs) following treatment (Fig. 1M).

However, Gene Ontology (GO) analysis highlighted a profound metabolic shift in post-treatment tumor cells, characterized by the upregulation of lipid transport

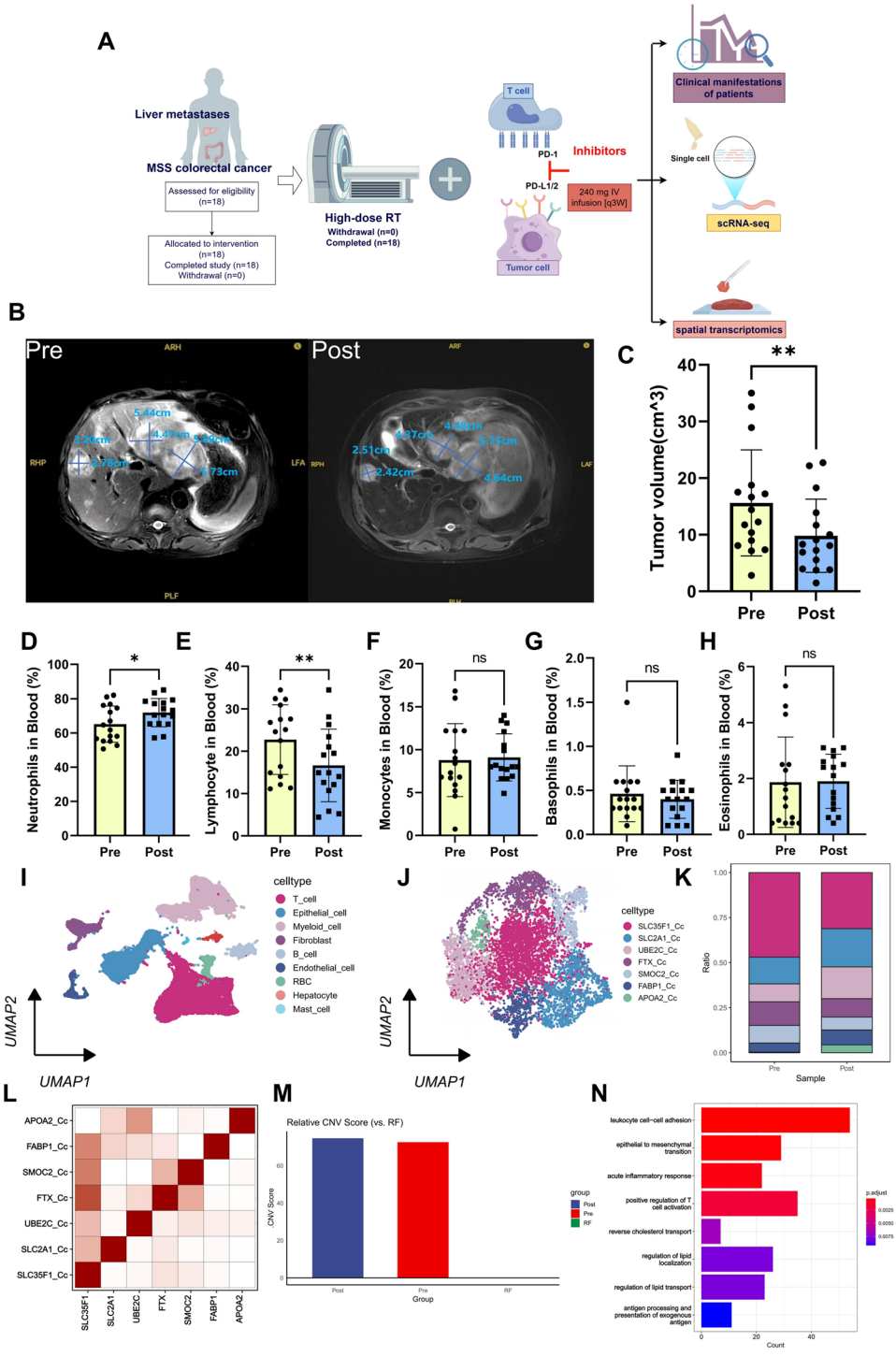

Fig. 1 (See legend on next page.)

and localization pathways (Fig. 1N). Simultaneously, we observed enrichment in antigen processing and T cell activation pathways. These data align with the established immunomodulatory role of RT in priming CD8 + T cell responses via tumor-associated antigen release, suggesting that treated tumor cells actively support adaptive immunity. Metabolic profiling further confirmed this reprogramming, showing enhanced fatty acid elongation, degradation, and ether lipid metabolism (Fig. S2C).

We specifically identified an APOA2-high tumor subpopulation (APOA2_Cc) that significantly expanded post-treatment (Fig. S2A-B). This cluster co-expressed

(See figure on previous page.)

Fig. 1 Clinical and molecular characterization of RT–ICI therapy in patients with CRC liver metastases.**A** Schematic overview of the patient cohort (n = 18) with microsatellite-stable (MSS) colorectal cancer liver metastases treated with high-dose radiotherapy (RT) followed by anti-PD-1 immune checkpoint inhibitors (ICI). Treatment regimen includes RT (3–5 fractions of 6–10 Gy) targeting 1–4 lesions, followed by PD-1 blockade (240 mg q3W). **B** Representative CT images showing regression of irradiated lesions (> 50% shrinkage) post-treatment. **C** Quantification of tumor burden changes pre- and post-RT–ICI. Tumor burden was measured before and after radiotherapy combined with immune checkpoint inhibitor (RT–ICI) treatment. Statistical significance was assessed using a paired two-tailed Student's t-test (n = 16). The trial enrolled 18 patients in total; however, due to clinical circumstances, not all data could be collected from every patient. This explains why certain analyses include fewer than 18 cases. **D**-**H** Flow cytometric analysis of peripheral blood immune cells, showing decreased lymphocytes and increased neutrophils post-treatment, with monocytes, eosinophils, and basophils unchanged. **I** UMAP visualization of 46,929 single cells from pre- and post-treatment tumor samples (scRNA-seq), annotated by major cell types. **J** UMAP of epithelial (tumor) cells with re-clustering into 7 subpopulations. **K** Relative abundance of tumor subpopulations pre- and post-treatment. **L** The heatmap shows the highly expressed marker genes in different tumor cell subsets. **M** Chromosomal copy number variation (CNV) analysis of tumor cells pre- and post-treatment, showing no significant differences (vs. hepatocytes reference). **N** Gene Ontology (GO) enrichment analysis of tumor cells post-treatment, highlighting upregulated lipid metabolic pathways and immune-related processes

key HDL-associated genes (APOA1, APOC1, APOC3) (Fig. S2D) and was positioned at the terminal trajectory of tumor evolution (Fig. 2A-B). High CNV levels relative to hepatocytes confirmed the malignant nature of these cells (Fig. 2C, Fig. S3A), and spatial transcriptomics validated their increased abundance in situ (Fig. 2D, Fig. S3B).

To link these intratumoral changes to systemic physiology, we examined biochemical parameters (Fig. 2E-N, Fig. S4). While post-treatment serum amylase decreased, HDL levels remained unchanged at the endpoint. We postulated a dynamic compensatory mechanism; indeed, longitudinal analysis revealed a transient yet significant spike in serum HDL during treatment (Fig. 2L). Thus, RT-ICI therapy appears to drive intratumoral APOA2 upregulation and HDL biogenesis, leading to transient systemic effects subject to homeostatic regulation.

RT–ICI combination therapy promotes infiltration of pro-inflammatory cytotoxic T cells

To determine whether tumor suppression was mediated by cytotoxic lymphocytes, we re-clustered T and NK cells from the single-cell dataset (Fig. 3A). Unsupervised analysis identified ten distinct subpopulations, which were annotated based on canonical marker genes (Fig. 3B, Fig. S5A–C). Among these, two effector T cell clusters exhibited high expression of GZMB and GZMK, respectively. While the proportion of GZMK$^+$ effector T cells (GZMK_Teff) remained unchanged after treatment, GZMB$^+$ effector T cells (GZMB_Teff) increased significantly (Fig. 3C–D). Notably, we identified a T cell cluster that expanded markedly following RT–ICI therapy. This population expressed high levels of pro-inflammatory chemokines and cytotoxic effector molecules, and was designated as inflammatory toxic T cells (IT_T) (Fig. 3E). Toxicity scoring confirmed that GZMB_Teff and IT_T exhibited the highest cytotoxic potential post-treatment (Fig. 3F), while inflammatory scoring indicated that IT_T displayed the strongest pro-inflammatory phenotype (Fig. 3G). Collectively, these results suggest that GZMB_Teff and IT_T cells contribute to anti-tumor responses following combination therapy.

To explore IT_T differentiation, we performed pseudotime trajectory analysis of T cell populations pre- and post-treatment (Fig. 3H). Post-treatment T cells formed a coherent developmental trajectory, whereas pre-treatment T cells displayed fragmented trajectories with multiple disconnected modules (Fig. S5D). In the post-treatment group, two dominant trajectories originated from CCR7$^+$ naïve T cells: one leading to cytotoxic T cells, and the other to FOXP3$^+$ regulatory T cells (Fig. 3I). Examination of exhaustion markers along pseudotime revealed that HAVCR2 and PDCD1 expression did not increase with T cell maturation, suggesting that RT–ICI therapy suppresses T cell exhaustion, consistent with the effects of immune checkpoint blockade (Fig. 3J). Conversely, multiple cytotoxic molecules showed progressive upregulation along the cytotoxic lineage trajectory (Fig. 3K). Analysis of exhaustion marker expression across patients pre- and post-treatment revealed no significant changes, indicating that RT–ICI therapy does not induce overt T cell exhaustion (Fig. S5E–H). Together, these findings indicate that RT–ICI therapy promotes differentiation of naïve-like memory T cells into inflammatory and cytotoxic effector states, thereby enhancing anti-tumor immunity.

To investigate whether tumor cells influence IT_T cells, we performed ligand–receptor interaction analysis between tumor cell subpopulations and IT_T cells. Multiple MHC-related genes were highly enriched among the top 20 tumor-derived ligands (Fig. 3L). Inhibitory MHC class I molecules, including HLA-E and HLA-G, were expressed in tumor cells, consistent with their role in immune evasion. In contrast, classical MHC class I genes such as B2M and HLA-A were expressed at higher levels relative to HLA-E/HLA-G (Fig. 3M). Binding potential analysis revealed strong predicted interactions between tumor cell-expressed MHC molecules and IT_T receptors, including CD8A, KLRD1, and KLRC3 (Fig. 3N). These results suggest that, following RT–ICI therapy, tumor cells may enhance antigen presentation to T cells via MHC–receptor interactions. This aligns with evidence that radiotherapy induces immunogenic cell death, facilitates the release of tumor-associated antigens, and

upregulates MHC class I expression, thereby enhancing tumor visibility to cytotoxic CD8⁺ T lymphocytes [18]. In this context, irradiated tumor cells may function as "in situ vaccines," promoting expansion and activation of effector T cells such as IT_T.

RT–ICI combination therapy promotes CETP⁺ M2-like macrophage polarization

Unsupervised clustering of single-cell transcriptomic data identified 11 myeloid subpopulations (Fig. 4A–B), including three conventional dendritic cell (cDC) subsets—cDC1 (XCR1⁺), cDC2 (CD1C⁺), and cDC3 (LAMP3⁺)—as well as FCN1⁺ monocytes and seven macrophage clusters: CETP_Ma, CXCL10_Ma, SPP1_Ma, APOC1_Ma, F13A1_Ma, GPR183_Ma, and MKI67_Ma (Fig. S6A). Among these, CETP_Ma infiltration increased markedly after treatment (Fig. 4C–D). Scoring with canonical macrophage activation signatures revealed that CETP_Ma displayed an immunosuppressive/tissue-remodeling program, whereas CXCL10_Ma exhibited a pro-inflammatory profile (Fig. 4E). CD163 [19], a marker of immunoregulatory macrophages, was elevated post-treatment, as confirmed by immunofluorescence staining and spatial transcriptomics (Fig. 4F–H).

Differential expression analysis revealed that CETP_Ma upregulated key genes associated with inhibitory or tissue-repair programs, including CD5L, CD163, TIMD4, CXCL12, and MRC1 (Fig. 4I). Gene ontology analysis showed enrichment for immune suppression and negative regulation of lymphocyte activation (Fig. 4J), as well as pathways such as "positive regulation of ERK1 and ERK2 cascade," previously linked to anti-inflammatory macrophage states via IL-4/STAT6 signaling and metabolic reprogramming [20]. Spatial transcriptomics confirmed co-localized expression of CETP and ARG1 in post-treatment tissues (Fig. S6B), indicating focal accumulation of CETP⁺ macrophages within the tumor microenvironment. Collectively, these data suggest that RT–ICI therapy promotes immunosuppressive, metabolically reprogrammed CETP⁺ macrophages, contributing to local immune modulation.

CETP⁺ macrophages sense HDL via LXR activation and correlate with poor prognosis

Given the post-treatment increase in APOA2⁺ tumor cells (Fig. 1J) and the central role of myeloid cells in lipid metabolism [21], we investigated whether myeloid populations modulate HDL homeostasis. Transcription factor activity inference revealed selective activation of NR1H3 (LXRα) and RXRA in CETP_Ma cells, suggesting that the LXR/RXR complex drives transcription of genes involved in cholesterol efflux, fatty acid metabolism, and inflammatory modulation, including CETP, CD5L, and MRC1 (Fig. S6C). CETP mediates HDL catabolism and has been associated with worse clinical outcomes in colorectal cancer [22,23]. These findings suggest a feedback loop in which RT–ICI therapy induces APOA2⁺ tumor cells to increase HDL production, sensed by LXR in CETP⁺ macrophages, promoting M2 polarization, CETP upregulation, and HDL clearance.

Pseudotime trajectory analysis indicated that CETP⁺ macrophages occupy late differentiation stages (Fig. 5B–C). Gene module analysis identified several modules preferentially enriched in CETP⁺ macrophages, with module 11 showing the strongest post-treatment upregulation and almost exclusive expression in this population (Fig. 5D–E). High expression of module 11 correlated with poor patient survival (Fig. 5F), highlighting the pathological relevance of CETP⁺ macrophages. Intercluster correlation analysis further revealed a functional axis linking CETP⁺ macrophages and APOA2⁺ tumor cells (Fig. 5G).

RT–ICI combination therapy reshapes Spatial and molecular cell–cell communication networks

To explore how combination therapy alters intercellular signaling dynamics, we performed cell–cell communication analysis across distinct cell populations before and after treatment. Globally, both the number and intensity of intercellular interactions increased significantly following RT–ICI therapy (Fig.S7A). Notably, CETP⁺ macrophages (CETP_Ma), inflammatory–toxic T cells (IT_T), and GZMB⁺ effector T cells (GZMB_T) exhibited markedly higher interaction strength with a broad range of other cell types post-treatment (Fig. 6A). Quantitative contribution analysis further revealed that IT_T and GZMB_T cells were major contributors to the overall signaling network after therapy, with both increased outgoing and incoming signal strengths (Fig.S7B).

We next assessed the signaling pathways driving these interactions. Among them, the CCL and CXCL chemokine pathways were substantially upregulated post-treatment (Fig.S7C). The enrichment of the CCL axis was attributed to high expression of CCL-family chemokines by IT_T cells, suggesting enhanced T cell-mediated recruitment (Fig.S8A). Detailed inspection of the CXCL network revealed strengthened interactions between CXCL10 and multiple T cell subsets (GZMB_T, GZMK_T, etc.), supported by upregulated ligand–receptor pairs such as CXCL9/CXCL10–CXCR3, known to mediate T cell recruitment and activation in inflamed tumors (Fig. 6B and Fig.S9A). In the spatial transcriptomics data, we observed co-localization of GZMB⁺ effector T cells (GZMB_Teff) and inflammatory-toxic T cells (IT_T) with tumor cells (Fig.S8B), along with co-localization of multiple CXCL10-CXCR3 ligand-receptor pairs (Fig.S8C).

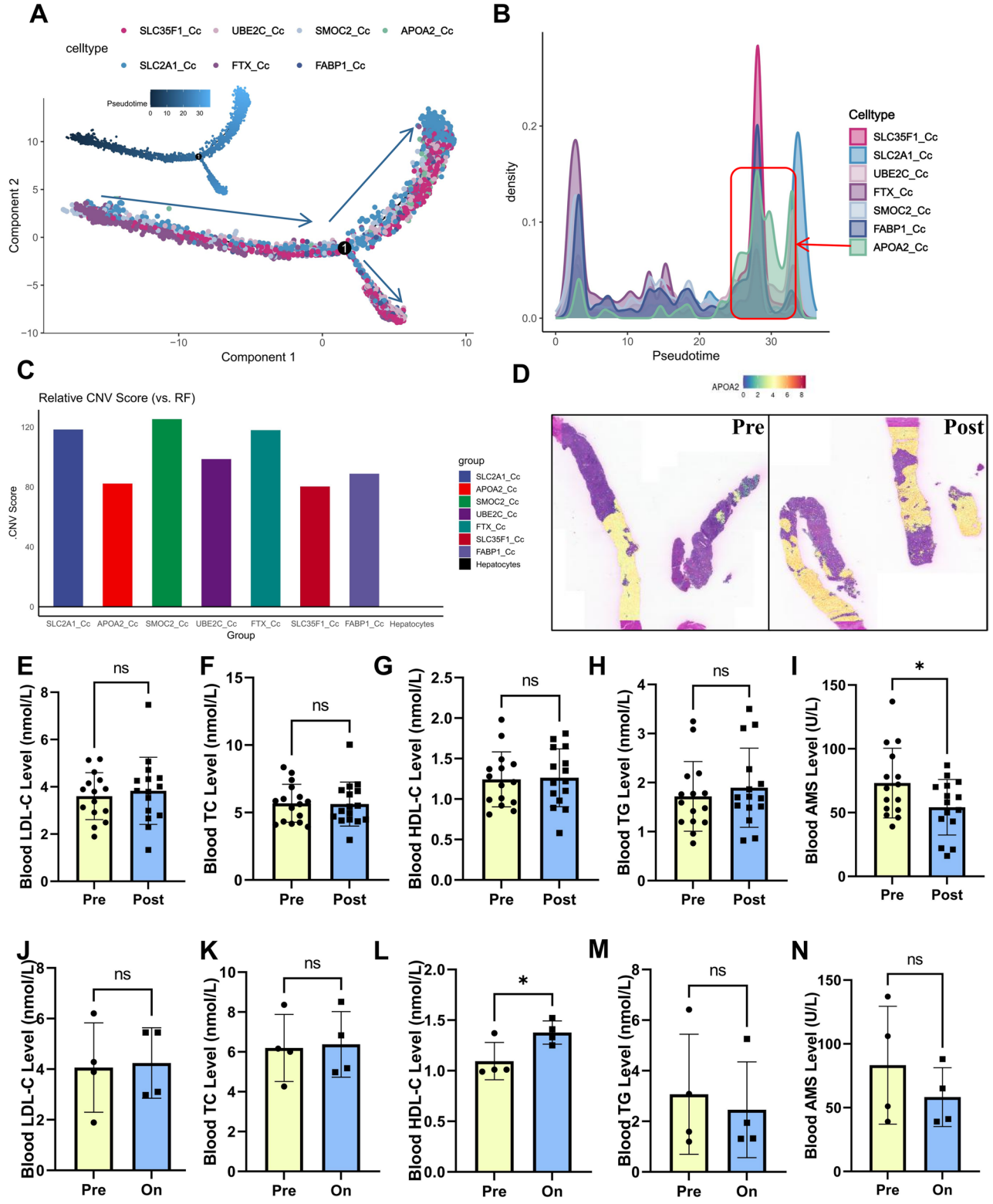

Fig. 2 RT–ICI induces APOA2⁺ tumor cells with enhanced lipid metabolism and systemic HDL modulation. **A** Pseudotime trajectory analysis of tumor cells constructed using aggregated data from all patients. The trajectory positions APOA2⁺ malignant cells at the terminal branch of the developmental continuum, indicating a treatment-associated shift toward this transcriptionally distinct state. **B** The density plot shows the distribution of different tumor cell subsets along the pseudotime. **C** Relative CNV scores of tumor subpopulations (vs. hepatocytes), showing higher CNV in APOA2⁺ cells. **D** Spatial transcriptomics confirming increased APOA2⁺ tumor cells post-treatment. The density of APOA2⁺ spots and the increase in signal intensity (darker red color indicating higher expression) clearly demonstrate an increase after therapy. **E**-**I** The bar chart shows the changes in various serum biochemical indicators before and after treatment. **J**-**N** The bar chart shows the changes in various serum biochemical indicators before and during treatment

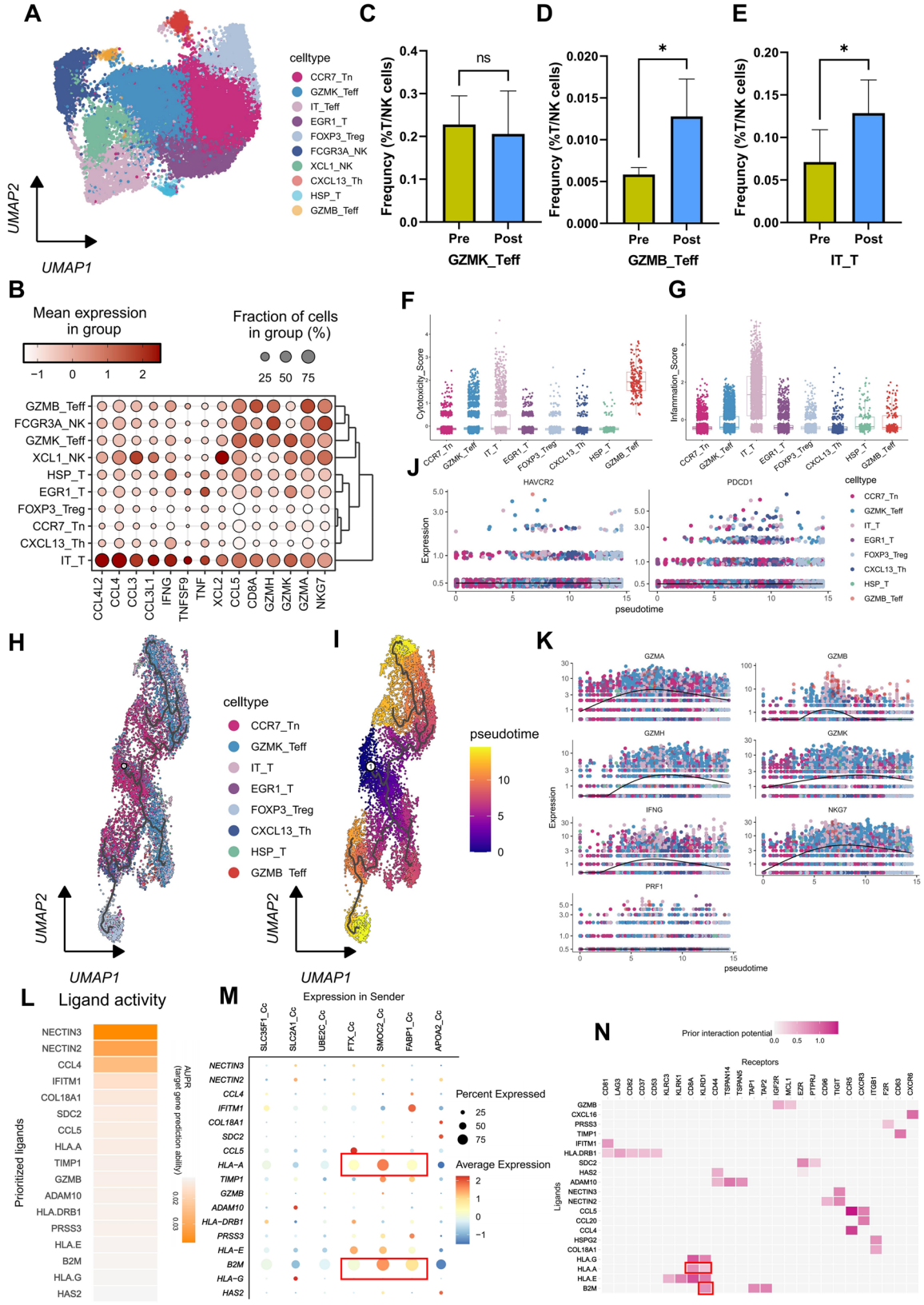

Fig. 3 (See legend on next page.)

(See figure on previous page.)

Fig. 3 Expansion of pro-inflammatory cytotoxic T cells post-RT–ICI. **A** UMAP of re-clustered T/NK cells, identifying 10 subpopulations. **B** Heatmap of canonical marker genes for T/NK subsets. **C**-**D** Increased proportion of GZMB⁺ effector T cells (GZMB_Teff) post-treatment, with GZMK_Teff unchanged. **E** Identification of inflammatory-toxic T cells (IT_T) characterized by high expression of pro-inflammatory chemokines and cytotoxic molecules, with marked expansion post-treatment. **F** Cytotoxicity scoring showing highest potential in GZMB_Teff and IT_T. **G** Inflammatory scoring highlighting IT_T as the most pro-inflammatory subset. **H**-**I** Pseudotime trajectory analysis of T cells, revealing unified differentiation paths post-treatment (naïve T cells → cytotoxic T cells/Tregs). **J** Expression dynamics of exhaustion markers along the pseudotime axis. **K** Expression dynamics of cytotoxic molecules along the pseudotime axis. **L** Top 20 ligand genes ranked by ligand activity from ligand–receptor interaction analysis. **M** Expression levels of ligand genes across various tumor cell subpopulations. **N** Heatmap showing the predicted binding affinity between ligands and their corresponding receptors

To validate these findings spatially, we applied RCTD-based deconvolution to Visium spatial transcriptomics data. Two annotation outcomes emerged: the first primarily identified stromal populations with limited immune cell resolution (Fig.S10A), while the second annotated diverse immune cell subsets (Fig.S10B). This discrepancy may stem from the co-localization of immune cells with dense stromal components in the tumor, along with the limited spatial resolution and capture efficiency of the 10x Visium platform—particularly for sparse or migratory immune cells.

Neighborhood enrichment analysis further revealed that CXCL10_Ma macrophages exhibited spatial proximity to multiple T cell subsets (Fig. 6C). Spatial visualization confirmed co-localization of CXCL10_Ma, IT_T, and GZMB_T populations (Fig. 6D), suggesting that macrophage-derived CXCL chemokines may directly recruit cytotoxic and inflammatory T cells to exert anti-tumor effects in situ. These findings highlight a reinforced pro-inflammatory circuit induced by RT–ICI therapy, coordinating innate and adaptive immunity within the tumor microenvironment.

Interestingly, CETP_Ma macrophages, despite being expanded post-treatment, showed consistently low neighborhood enrichment scores across cell types (Fig. 6E). Spatial mapping revealed that, although CETP_Ma infiltration increased post-therapy (in agreement with scRNA-seq data), these cells were predominantly located outside of the irradiated tumor region (Fig. 6F). Given our earlier observation of transient HDL elevation in circulation after radiotherapy, we hypothesize a systemic feedback mechanism: radiotherapy enhances APOA2⁺ tumor cell–derived HDL production, which circulates and activates LXR signaling in distant macrophages, leading to M2 polarization and CETP⁺ macrophage expansion. This phenomenon, which we term a "distal immunometabolic effect", may contribute to tumor immune evasion and outgrowth in non-irradiated sites. These results underscore a dual nature of RT–ICI–induced systemic remodeling: while promoting anti-tumor immunity locally, it may simultaneously facilitate immunosuppressive niches at distant sites via metabolic rewiring.

Discussion

In this study, we systematically dissected the immunometabolic landscape of colorectal cancer (CRC) liver metastases under RT–ICI combination therapy using single-cell RNA sequencing and spatial transcriptomics. Our findings highlight a dual impact of this treatment strategy: it locally enhances anti-tumor immunity while simultaneously inducing a distal immunometabolic remodeling program that may modulate systemic immune responses.

A major discovery was the emergence of an APOA2⁺ tumor cell subpopulation after RT–ICI therapy. These cells exhibited elevated lipid metabolism, including enhanced fatty acid elongation, ether lipid synthesis, and reverse cholesterol transport. The upregulation of APOA2 and associated HDL pathway genes (e.g., APOA1, APOC1, APOC3) suggests a therapy-induced reprogramming of tumor lipid metabolism. Given prior studies linking CNVs to tumor aggressiveness, this suggests that RT–ICI therapy does not substantially alter tumor malignancy at the genomic level [24]. Functionally, this metabolic shift correlated with improved antigen processing and presentation capacity, reinforcing the idea that RT not only causes direct tumor cytotoxicity but also primes tumor cells as "in situ vaccines" to activate adaptive immunity.

In line with this, we observed significant expansion of two key cytotoxic T cell subsets—GZMB⁺ effector T cells (GZMB_Teff) and inflammatory-toxic T cells (IT_T)—after treatment. These populations demonstrated high cytotoxic and inflammatory activity and were spatially co-localized with antigen-presenting tumor cells and chemokine-producing macrophages (CXCL10_Ma), suggesting the formation of coordinated immune hubs in the tumor microenvironment. Notably, pseudotime analysis confirmed that post-treatment T cells followed a unified differentiation trajectory toward cytotoxic or regulatory states, while pre-treatment cells exhibited disorganized developmental programs. Importantly, exhaustion markers (PDCD1, HAVCR2) did not increase during this transition, indicating sustained T cell function under RT–ICI therapy.

Paradoxically, our data also revealed the expansion of CETP⁺ M2-like macrophages (CETP_Ma)—an immunosuppressive myeloid population—following treatment. CETP_Ma expressed high levels of canonical M2 markers

(CD163, MRC1), immunosuppressive genes (TIMD4, CXCL12), and LXR target genes (CETP, CD5L), and exhibited enrichment in pathways such as ERK1/2 signaling and negative regulation of lymphocyte activation. These molecules are well-established mediators of M2 polarization: CD5L (AIM) promotes lipid accumulation and enhances anti-inflammatory macrophage polarization [25]. CD163, a scavenger receptor, is a prototypical M2 marker involved in hemoglobin clearance and IL-10 production [26]. TIMD4 (TIM4), often associated with phagocytic clearance of apoptotic cells, contributes to a tolerogenic macrophage phenotype [27]. CXCL12 (SDF-1) facilitates immune suppression by recruiting regulatory T cells and M2-like macrophages [28]. MRC1 (CD206), a mannose receptor, promotes tissue repair and is upregulated during alternative macrophage activation [29]. Transcription factor analysis pinpointed selective activation of LXRα (NR1H3) and RXRA in this subset, suggesting that circulating HDL—elevated transiently during treatment—activates the LXR/RXR axis in macrophages, promoting their polarization toward an M2-like state.

Strikingly, spatial transcriptomics revealed that CETP_Ma was predominantly localized outside irradiated tumor regions. Coupled with the transient rise in serum HDL levels post-RT, this led us to propose a "distal immunometabolic effect": RT-induced HDL from APOA2$^+$ tumor cells circulate to distant sites, where it engages LXR signaling in macrophages, inducing CETP expression and M2 polarization. This may facilitate immune suppression and tumor growth at non-irradiated lesions, representing a potential mechanism of systemic immune escape despite local immune activation.

Our results have both mechanistic and translational implications. First, they highlight the metabolic-immune crosstalk initiated by RT–ICI therapy, revealing how tumor-derived lipid cues can shape systemic immunity. Second, the identification of CETP_Ma as a spatially distinct, prognostically adverse population suggests that targeting the HDL–LXR–CETP axis may mitigate unintended immunosuppression and improve treatment efficacy. Third, the spatial co-localization of CXCL10_Ma, IT_T, and GZMB_Teff underscores the therapeutic value of reinforcing localized immune hubs while minimizing distal immune dampening.

However, this study has several limitations. The sample size, though prospectively collected and paired, remains modest ($n = 18$), which may limit the generalizability of certain findings. Second, while our spatial transcriptomic analysis revealed key cellular relationships, the limited resolution of the 10x Visium platform—especially in densely fibrotic liver tissue—may underestimate immune cell infiltration. Third, while we inferred LXR activation based on gene expression and regulon analysis, functional validation (e.g., ChIP–seq or LXR inhibition assays) is warranted to confirm causality. Lastly, the precise role of CETP$^+$ macrophages in promoting distal immune escape remains to be tested in vivo, possibly through lineage tracing or HDL transfer models. In this study, activation of the HDL–LXR–CETP axis was consistently observed across multiple patient subsets. Among the 18 patients enrolled in the phase I trial, paired plasma samples during treatment were available for only 4 individuals, all of whom showed increased HDL levels following RT–ICI therapy. In parallel, single-cell and spatial transcriptomic profiling performed in another 4 patients demonstrated enrichment of APOA2$^+$ tumor cells and induction of downstream LXR–CETP–associated metabolic programs within the tumor microenvironment. Together, these convergent observations across 8 patients support the presence of therapy-induced HDL metabolic remodeling in a subset of MSS CRC patients. Nevertheless, because additional biospecimens from the remaining trial participants were not accessible, further studies in larger cohorts will be required to determine the broader prevalence and clinical significance of this metabolic axis.

In summary, our study reveals that RT–ICI therapy orchestrates a complex immunometabolic reprogramming in CRC liver metastases, characterized by localized T cell activation and distal macrophage-mediated immune modulation. These findings underscore the need to consider spatial and metabolic heterogeneity in immunotherapy response, and they nominate the HDL–LXR–CETP axis as a potential target to synergize with RT–ICI therapy and overcome distal resistance.

Materials and methods

Patient samples

Paired tumor samples were obtained from three patients with colorectal cancer liver metastases (CRLM) undergoing radiotherapy combined with immune checkpoint inhibitor (RT–ICI) therapy. Tumor tissues were collected before and after RT–ICI treatment. One of the post-treatment tumor samples was additionally processed for spatial transcriptomics analysis. All tissue collections were performed under institutional guidelines, and samples were immediately placed on ice and processed for downstream applications. Fresh tumor tissues were mechanically and enzymatically dissociated into single-cell suspensions using a cocktail of collagenase IV and DNase I at 37 °C for 30–45 min with gentle agitation. Cell suspensions were filtered through a 40 μm mesh and washed with PBS containing 0.04% BSA. Cell viability was assessed by trypan blue staining, and only samples with >85% viability were processed. Single-cell libraries were prepared using the DNBelab C Series High-Throughput Preparation Kit Set Kit V3.0 (TaiM 4) and MobiCube High-throughput Single Cell 3' Transcriptome

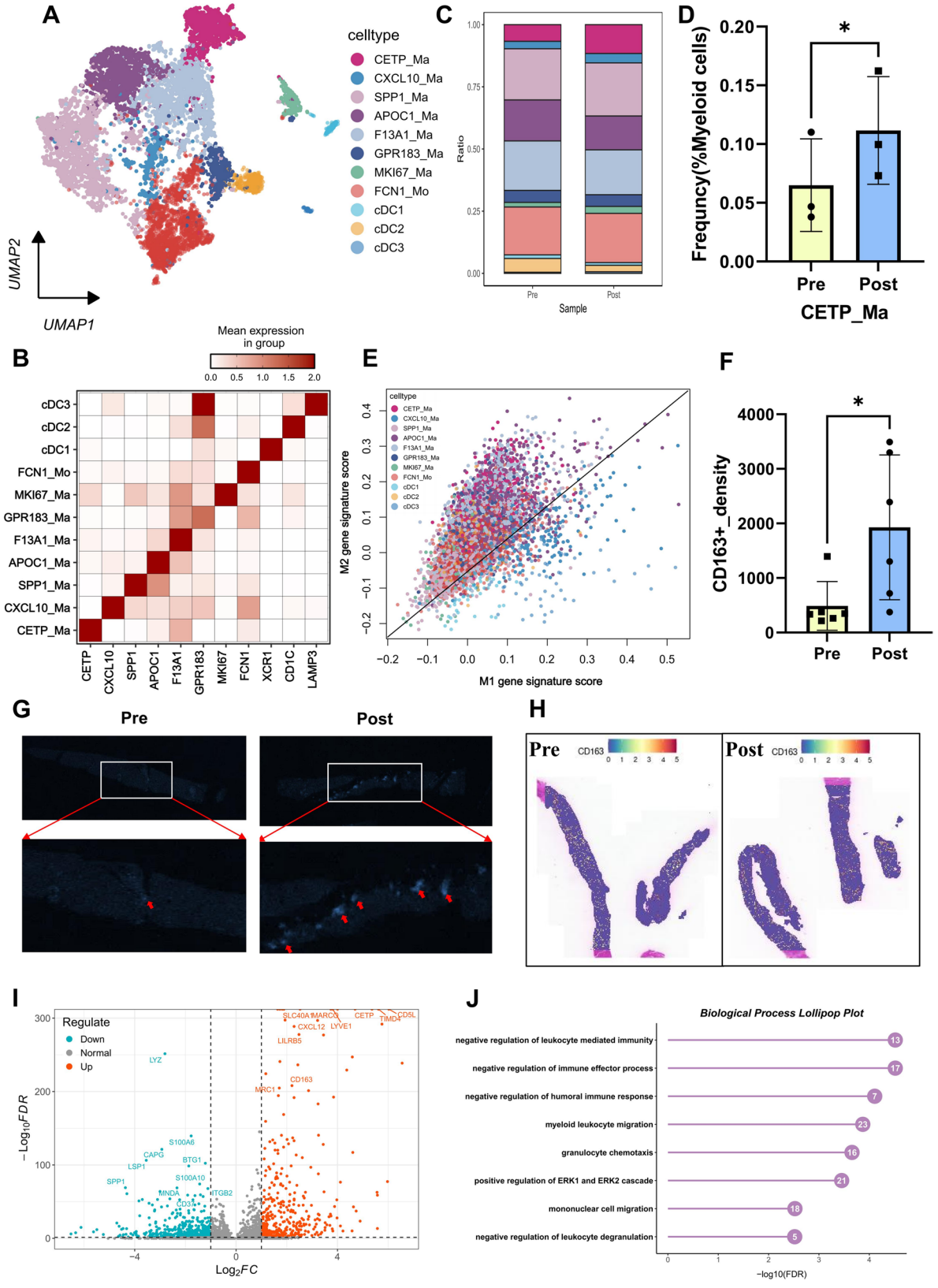

Fig. 4 (See legend on next page.)

(See figure on previous page.)

Fig. 4 Polarization of CETP⁺ M2-like macrophages in response to RT–ICI.**A** UMAP of re-clustered myeloid cells, identifying 11 subpopulations (3 cDC subsets, FCN1⁺ monocytes, 7 macrophage clusters). **B** Heatmap of marker genes for myeloid subsets (e.g., CETP⁺, CXCL10⁺, SPP1⁺ macrophages). **C**-**D** Post-treatment, we observed increased infiltration of CETP⁺ macrophages (CETP_Ma). Statistical significance was assessed using paired t-tests, comparing the proportion of CETP⁺ macrophages among total macrophages for each patient before and after treatment based on single-cell RNA-seq data (n = 3). **E** M1/M2 signature scoring, showing CETP_Ma with high M2-like and CXCL10_Ma with high M1-like profiles. **F** Bar plot showing the density of CD163⁺ cells as determined by immunofluorescence analysis. Paired t-tests were used to compare the percentage of CD163⁺ cells within equivalently sized tumor regions across six patients before and after treatment. **G** Immunofluorescence staining confirms increased expression of CD163, a marker of M2 macrophages, following treatment. **H** Spatial transcriptomic analysis further reveals elevated CD163 expression after treatment, consistent with enhanced M2 polarization. **I** Volcano plot showing differentially expressed genes between CETP⁺ macrophages and other myeloid cell subsets. **J** GO enrichment analysis highlights upregulated pathways in CETP⁺ macrophages

Set V2.1(cat.no.PN-S050200301)according to the manufacturer's instructions. Briefly, single cells were encapsulated into Gel Bead-in-Emulsions (GEMs), and reverse transcription was performed to generate barcoded cDNA. Amplified cDNA libraries were constructed and sequenced on an BGI DNBSEQ-T7 PE150 platform to achieve a minimum of 50,000 reads per cell. One post-treatment CRLM tumor sample was fixed in 4% PFA and paraffin embedding and cryosectioned at 5 μm thickness. Tissue sections were placed onto 10x Genomics Visium HD gene expression slides and imaged using brightfield microscopy. Permeabilization, reverse transcription, and library preparation were performed according to the manufacturer's protocol. The resulting libraries were sequenced on an BGI DNBSEQ-T7 sequencing platform to achieve a depth of approximately 300 million reads per tissue section. Raw sequencing data were processed using Cell Ranger (v7.1, 10x Genomics) to generate gene-cell count matrices for scRNA-seq and spatial transcriptomics datasets. For scRNA-seq, low-quality cells with < 200 detected genes or > 10% mitochondrial gene expression were excluded. For spatial transcriptomics, spots with low unique molecular identifier (UMI) counts were filtered out. Downstream analyses, including normalization, dimensionality reduction, clustering, and visualization, were performed using the Seurat R package (v5.1). The blocks for spatial transcriptomics (ST) were prepared by the conventional method for preparing paraffin specimens. Briefly, fresh tissues were obtained from patients and immediately fixed in 4% paraformaldehyde. Then dehydration and wax immersion were performed for the fixed samples. Subsequently the wax-soaked tissue is embedded in the embedding machine. Paraffin sections of 5 μm were prepared using the Leica RM2235 manual rotary slicer (Leica Microsystems, Germany). Paraffin sections containing the target area were attached to the slide (Sigma-Aldrich, P0425). Subsequent dewaxing, HE staining and cross-linking were carried out in accordance with the experimental standard procedure of 10xGenomics (CCG000684). Referring to the experimental procedure of 10x Genomics (CG000685), 10x GenomicsVisium HD slides were used (10x Genomics, catalog number: PN-2000970) Probe hybridization, CytAssist film transfer and library construction were performed with PN-2,000,970 and Visium HD Spatial Gene Expression Reagent Kits (human: PN-1000675; mouse: PN-1000676). The final library was sequenced using the BGI DNBSEQ-T7 sequencing platform with 100 bp at both ends.

Peripheral blood mononuclear cell analysis by flow cytometry

The blood was captured from the enrolled patients and was conducted by Sysmex XN-9100 Fully automatic blood cell analysis assembly line, which is approved with SOP in our hospital. The line consists of three XNS, one PA-990 C, one SP-10, Input/Output specimen stages and tracks. The obtained whole blood was mixed upside down and then tested on the machine with the matched staining solution for blood cell analysis. The test data is directly transmitted to the indoor quality control system. Only after being confirmed by the quality control system every day can the specimens be tested. Confirm whether the indoor quality control data is within the allowable range in accordance with the project SOP (Standard Operating Procedure). The process has been approved in our hospital, and the study was approved by the Ethics Committee of Jiangsu Cancer Hospital (approval ID: 2023-046, 2024-099) and was designed and conducted in accordance with the Declaration of Helsinki and ethical guidelines for clinical research. All participants provided written informed consent. The study is registered on ClinicalTrials.gov (Identifier: NCT06045286).

Fresh peripheral blood samples were collected from patients with colorectal cancer liver metastases (CRLM) into EDTA-coated tubes and processed within 2 h of collection. Red blood cells were lysed using ammonium-chloride-potassium (ACK) lysis buffer, and the remaining leukocytes were washed and resuspended in PBS containing 2% fetal bovine serum (FBS). Immune cell populations were quantified using a standard flow cytometry panel. Granulocytes, lymphocytes, and monocytes were identified based on forward and side scatter properties, and eosinophils and basophils were further distinguished using specific surface markers. Flow cytometry acquisition was performed on a BD FACSCanto II cytometer (BD Biosciences), and data were analyzed using FlowJo

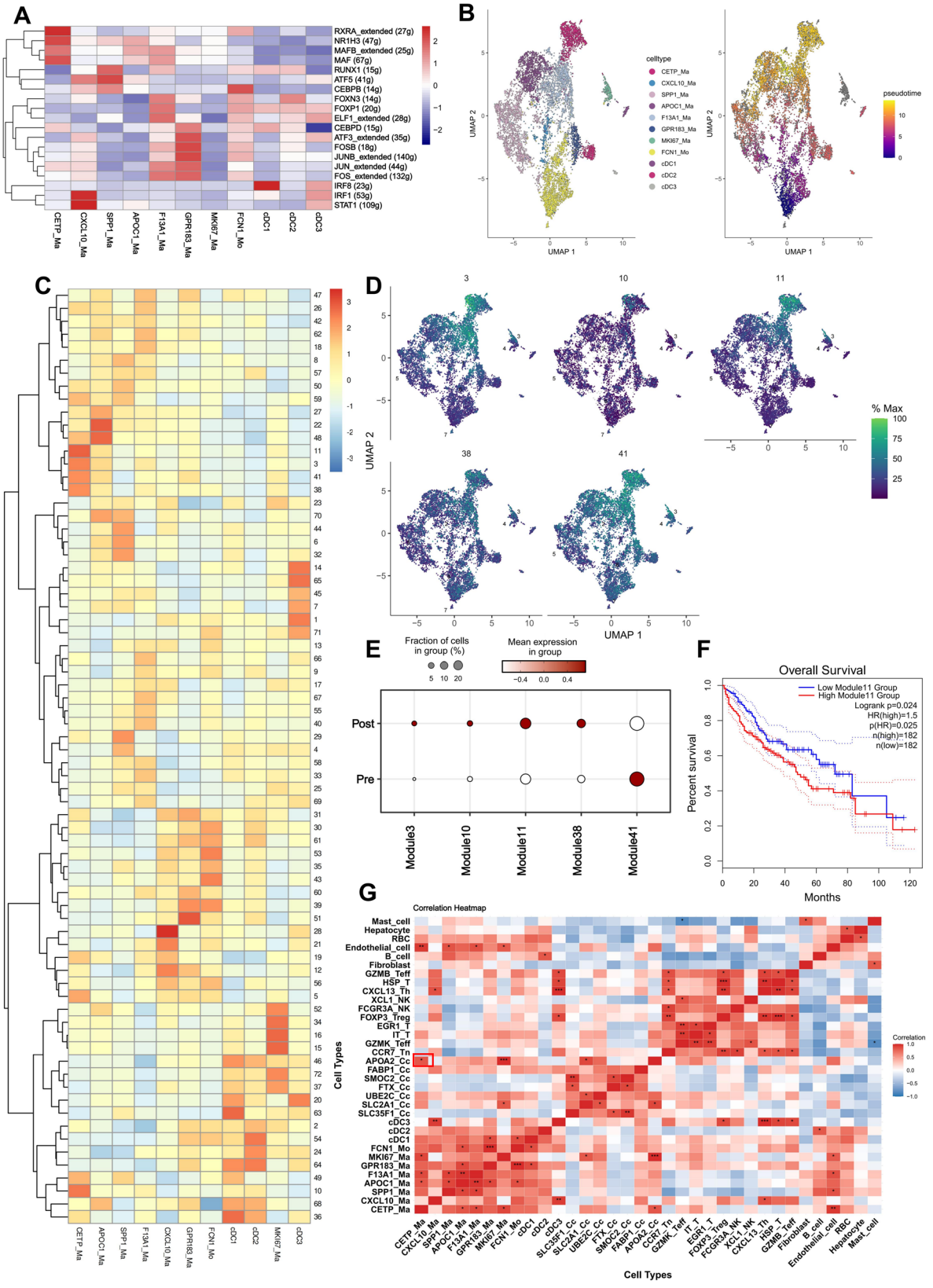

Fig. 5 (See legend on next page.)

(See figure on previous page.)

Fig. 5 CETP$^+$ macrophages sense HDL via LXR/RXR and associate with poor prognosis. (**A**) Transcription factor activity analysis in myeloid cells, showing selective activation of LXRα (NR1H3) and RXRA in CETP_Ma. (**B**) Pseudotime trajectory of myeloid cells, with CETP_Ma at the terminal (highly differentiated) stage. (**C**) Heatmap showing the expression of gene modules across myeloid cell subsets. (**D**) Feature plots illustrating the spatial expression of gene modules in myeloid populations. (**E**) Dot plot depicting gene module expression levels before and after treatment. (**F**) Kaplan-Meier survival analysis showing association of high module 11 expression with worse prognosis. (**G**) Correlation heatmap of myeloid subsets, highlighting strong association between CETP_Ma and APOA2$^+$ tumor cells

software (v10.8). Cell populations were reported as percentages of total leukocytes.

Immunofluorescence

Formalin-fixed, paraffin-embedded fine-needle biopsy specimens from paired samples were sectioned at 4 μm. Sections were deparaffinized, rehydrated, and subjected to heat-induced antigen retrieval in citrate buffer (pH 6.0). After blocking with Antibody Diluent (Agilent Technologies) for 15 min, the slides were incubated with the primary antibody against CD163 (ab189915, Abcam) for 30 min at 37 °C. After washing, sections were incubated with an HRP-conjugated secondary antibody (PV-8000, ZhongShan Golden Bridge) for 10 min, followed by fluorescent signal development using the corresponding fluorophore. Nuclei were counterstained with DAPI, and slides were mounted with ProLong Gold Antifade reagent (Thermo Fisher Scientific). Stained sections were scanned using the TissueFAXS SL panoramic tissue imaging system (version 7.1.120). Tissue segmentation, single-cell identification, and quantification of CD163 expression were performed using StrataQuest software (version 7.1.129). CD163 positivity was defined based on predetermined intensity thresholds, and the percentage of CD163$^+$ cells was calculated as the number of CD163-positive cells divided by the total number of nucleated cells within each section.

Single-cell RNA-seq data quality control

We performed stringent quality control on the single-cell RNA sequencing (scRNA-seq) data using the Seurat [30] package (v5.2.1). Cells with a mitochondrial gene percentage greater than 20% or with the number of detected genes (nFeature_RNA) less than 200 or greater than 7500 were excluded to eliminate low-quality or potential doublet cells with abnormally high complexity. Furthermore, cells expressing marker genes from more than two distinct cell types were classified as putative doublets and removed from downstream analysis. After these filtering steps, a total of 46,929 high-quality cells were retained for further investigation.

Survival analysis

Survival analysis was conducted using GEPIA2 [31] (http://gepia2.cancer-pku.cn/#survival), a web-based tool that integrates TCGA and GTEx data. The "Group Cutoff" parameter was set to "Median," allowing samples to be dichotomized into high and low expression groups based on the median expression of the gene of interest. Kaplan–Meier survival curves were generated, and statistical significance was assessed using the log-rank test.

Unsupervised clustering and cell type annotation

We performed unsupervised clustering and cell type annotation using the Seurat package (v5.2.1). Raw count matrices were normalized and variance-stabilized using the SCTransform function, which employs regularized negative binomial regression to model technical noise and improve biological signal detection. To mitigate potential batch effects among different samples, we applied Harmony [32] (v0.1.1), an integration algorithm that aligns shared cell types across conditions while preserving biological variation. Principal component analysis (PCA) was conducted on the corrected data, followed by shared nearest neighbor (SNN) graph construction and Louvain clustering. UMAP was used for two-dimensional visualization of the cellular landscape. Cell types were assigned based on the expression of canonical marker genes and validated by differential expression analysis using the FindMarkers function.

Inference of chromosomal copy number variations (CNVs)

Chromosomal copy number variation (CNV) analysis was performed using the inferCNV [33] R package (v1.22.0), which infers large-scale CNVs at single-cell resolution from scRNA-seq data by comparing gene expression patterns across genomic coordinates. Tumor epithelial cells were analyzed as the observation group, and a subset of reference "normal" cells (mast cell) was used to estimate the baseline expression.

The gene expression matrix was first filtered and log-transformed as required by the package. Genes were then ordered based on their genomic positions according to the human genome annotation (GRCh38). A denoising step was applied using a sliding window approach to smooth expression patterns across neighboring genes. CNV scores were visualized as a heatmap, where gains and losses in chromosomal regions are reflected by consistent upregulation or downregulation of gene expression, respectively.

Pseudotime trajectory analysis

To infer the developmental trajectories of specific cell populations, we performed pseudotime analysis using the

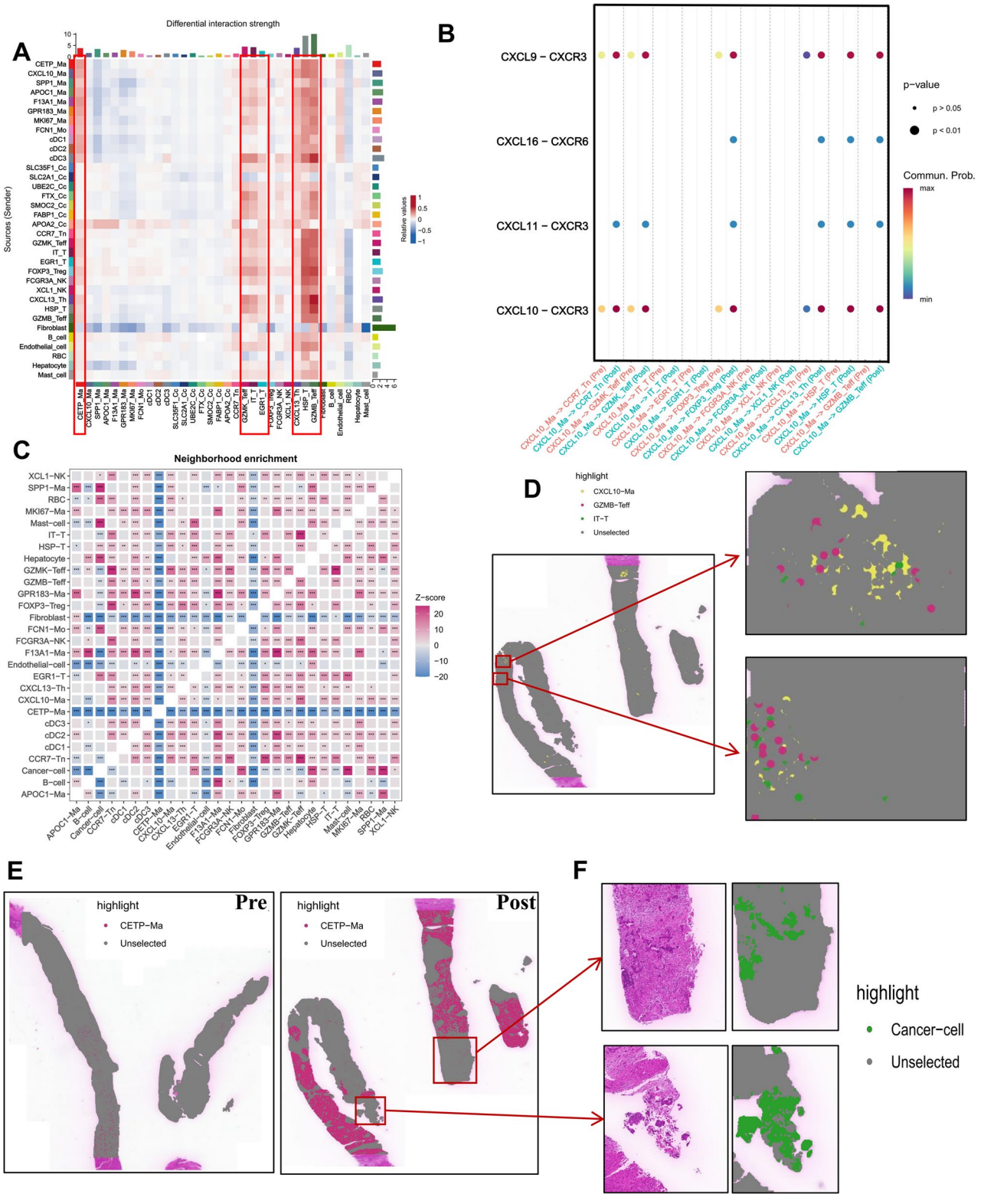

Fig. 6 Reinforced cell-cell communication and spatial coordination of immune cells.**A** Heatmap showing the strength of cell–cell interactions among different cell subsets. **B** Dot plot illustrating ligand–receptor interactions within the CXCL chemokine signaling network pre- and post-treatment. **C** Neighborhood enrichment analysis showing spatial proximity of CXCL10⁺ macrophages to T cell subsets (IT_T, GZMB_Teff). **D** Spatial co-localization of CXCL10_Ma, IT_T, and GZMB_Teff visualized by RCTD deconvolution of Visium data. **E**-**F** Spatial mapping of CETP_Ma, showing expanded infiltration post-treatment but preferential localization to non-irradiated tumor regions, consistent with "distal immunometabolic effect"

Monocle3(v1.3.7) and Monocle2(v2.24.0) R package [34]. The integrated and batch-corrected Seurat object was first converted into a cell_data_set (CDS) object using the as.cell_data_set() function. Dimensionality reduction was carried out using the reduce_dimension() function with the UMAP algorithm, followed by cell clustering and trajectory graph learning via the cluster_cells() and learn_graph() functions, respectively.

We designated the root of the trajectory as naïve-like or progenitor-like cells based on marker gene expression (e.g., CCR7, TCF7), and pseudotime was assigned to each cell using the order_cells function. Gene expression dynamics along the pseudotime axis were visualized using plot_genes_in_pseudotime. Cells with longer pseudotime values were considered more differentiated. This approach enabled us to reconstruct lineage relationships and dynamic transcriptional changes across cellular states before and after RT–ICI treatment.

Gene module analysis

To characterize co-regulated gene programs within myeloid populations, we performed gene module analysis using the find_gene_modules() function from the Monocle3 R package (v1.3.1).

Transcription factor activity analysis

We performed transcription factor (TF) activity inference using the R implementation of the SCENIC [35] pipeline (version 1.3.1), which integrates GENIE3, RcisTarget, and AUCell to reconstruct gene regulatory networks and assess regulon activity at single-cell resolution. Raw UMI count matrices were used as input, and gene filtering was first applied to retain genes expressed in at least 1% of cells. Co-expression modules were identified using GENIE3, which predicts TF–target relationships based on random forest regression. These modules were then refined using RcisTarget with motif databases (hg38), to identify direct target genes with enriched TF-binding motifs, resulting in high-confidence regulons. To quantify regulon activity across cells, we used AUCell, which calculates the area under the recovery curve (AUC) for the expression of each regulon's target genes per cell. The resulting AUC matrix was normalized and visualized using UMAP and violin plots with Seurat. We focused particularly on regulons with high activity in $CETP^{+}$ macrophages.

Cell–cell communication analysis

To investigate intercellular communication between tumor cells and immune cells, we applied the CellChat [36] package (v1.6.1) in R. CellChat infers ligand–receptor interactions and visualizes signaling networks based on single-cell transcriptomic data. We constructed a CellChat object using normalized gene expression data and predefined cell-type annotations. We first filtered lowly expressed genes and used the CellChatDB.human database to retrieve known ligand–receptor pairs. The communication probability between cell types was computed using a mass action–based model that integrates both expression levels and the number of expressing cells. We identified significant signaling pathways and quantified incoming and outgoing interaction strengths per cell type. To explore treatment-induced changes, we performed comparative analysis between pre-treatment and post-treatment samples using identifyOverExpressedInteractions and computeCommunProbPathway functions. Network centrality analysis was applied to identify key signaling hubs.

To further explore how tumor cell subpopulations may influence the gene expression programs of IT_T cells, we applied NicheNet [37] (R package v1.1.0), a computational method that models ligand–receptor–target gene interactions by integrating prior knowledge of signaling and gene regulatory networks. We designated tumor cells as the sender population and IT_T cells as the receiver population. Differentially expressed genes (DEGs) in IT_T cells after treatment were identified using the Seurat FindMarkers function, with thresholds set at $\log_2FC > 0.25$ and adjusted $P < 0.05$. These DEGs were used as the target gene set in NicheNet's prioritization model. NicheNet ranks candidate ligands based on their ability to predict the observed transcriptional changes in the receiver population. We calculated ligand activities using the Pearson correlation between ligand-regulated target gene predictions and actual expression changes in IT_T cells. Top-ranked ligands were visualized using the nichenet_seuratobj_aggregate function.

Gene signature scoring

To quantify the activity of predefined gene sets at the single-cell level, we applied the AddModuleScore function from the Seurat package (v5.2.1). This method computes the average expression of a gene set in each cell, subtracted by the aggregated expression of control gene sets matched for expression bin, thereby providing a robust score that reflects gene set activation independent of library size and cell-to-cell expression variability. We applied this scoring approach to evaluate a variety of cellular programs, including M1/M2 macrophage polarization (M1:CXCL9, CCL19, CXCL10, IDO1, EBI3, TNFAIP6, CCR7, LAMP3, CCL5, CD40, IRF8, CD38, CCL4, APOL3, CXCL11, ADAMDEC1, HCK, BCL2A1, RSAD2, CYP27B1, KYNU, SIGLEC1, SLAMF1, SLC2A6, IFI44L, SAMSN1, LILRB2, TLR2, CCL8, APOBEC3A, AQP9, C3AR1, HLA-DQA1, MNDA, IL2RA, SLC15A3, CD80, ADGRE1, CHI3L1, RASSF4, IL4R, AIM2, PLA1A, MMP9, TLR8, HESX1, SOCS1, LST1, NOD2, IL7R, FLVCR2, BIRC3, PTGIR, CHI3L2, PLA2G7,

GPR183, AIF1, CD4, HLA-DOB, MSC, ADGRE2, CCR5, CLEC2D, TNFRSF4, CD86, SPIB, LAG3, DHX58, CLIC2, ACHE, CCL18, LY86, CCL14, TNIP3, MMP25, ACP5, APOBEC3G. M2:MMP9, MS4A6A, CCL18, AIF1, NCF2, CD4, CLEC4A, CCL13, LY86, SLC15A3, CLEC10A, CCL23, HLA-DQA1, RNASE6, ADAMDEC1, HCK, NPL, TREM2, IRF8, SIGLEC1, CCL4, SAMSN1, CLEC7A, TLR2, P2RY13, CCL8, CD86, CD180, CD68, CD209, C3AR1, GPR183, CCL14, DPEP2, FPR3, CD37, LST1, CLIC2, HRH1, EGR2, CHI3L1, CFP, C5AR1, MNDA, PTGER2, CD300A, PIK3IP1, IGSF6, RENBP, PLA2G7, FCGR2B, SLAMF8, RASGRP3, QPCT, LILRB2, ATP8B4, PTGIR, FRMD4A, TLR8, KYNU, CHST15), T cell cytotoxicity(GZMB, GZMH, GZMK, GZMA, TIA1, PRF1, LAMP1, GNLY, FASLG, SLAMF7, ZAP70, CD69, TNF) and inflammatory responses(CCL4L2, CCL4, CCL3, CCL3L1, IFNG, XCL2, XCL1, CCL5, TNFSF9, TNF, CXCL10, CXCL9). Gene sets were curated from established immune signatures reported in the literature, and adapted where necessary for species-specific or context-specific relevance. The resulting module scores were then visualized using violin plots, feature plots, and UMAP overlays to compare gene set activation across conditions and cell states.

Visualization

All data visualizations were performed using a combination of R packages tailored for high-resolution and customizable graphics. The ggplot2 package (v3.4.2) served as the primary tool for generating violin plots, boxplots, bar plots, and scatter plots, offering a flexible grammar of graphics for presenting single-cell features across different conditions and cell types. For heatmap generation, we utilized the pheatmap package (v1.0.12), which enabled hierarchical clustering and intuitive visualization of gene expression or signature scores across cell subsets. Dimensionality reduction plots, including UMAP and t-SNE visualizations, were generated using the Seurat package (v5.2.1), which integrates clustering and annotation with effective graphical outputs for single-cell datasets. In addition, we employed scRNAtoolVis for summarizing key quality control metrics (e.g., gene and UMI counts, mitochondrial content) and for visualizing cell-type distributions, batch effects, and clustering outcomes. This package allowed rapid inspection of sample integration quality and supported interactive exploration of marker gene expression.

Differential expression and enrichment analyses

Differential gene expression analysis between specific cell populations or experimental groups was performed using the FindMarkers function from the Seurat package (v5.2.1). We applied the Wilcoxon rank-sum test by default and considered genes as differentially expressed if they met the following criteria: an adjusted P-value < 0.05 (Benjamini–Hochberg correction) and an absolute $\log_2$(fold change) > 0.3. To avoid spurious results from lowly expressed genes, we filtered out genes expressed in fewer than 10% of cells in either group. To interpret the functional implications of differentially expressed genes (DEGs), we conducted Gene Ontology (GO) and Kyoto Encyclopedia of Genes and Genomes (KEGG) pathway enrichment analyses using the enrichGO and enrichKEGG functions from the clusterProfiler package (v4.10.0). The org.Hs.eg.db annotation package (v3.18.0) was used to map gene symbols to Entrez IDs for human gene ontology analysis. Terms with adjusted P-values < 0.05 were considered significantly enriched. Results from enrichment analyses were visualized using dot plots, bar plots, and enrichment maps generated by clusterProfiler's built-in functions, enabling a comprehensive interpretation of the biological processes and pathways enriched in each comparison.

Spatial transcriptomics deconvolution

To estimate the cell-type composition across spatial transcriptomics spots, we applied the Robust Cell Type Decomposition (RCTD) method as implemented in the SpaceXr package [38] (v2.2.1). RCTD enables probabilistic mapping of single-cell references onto spatial transcriptomic data by modeling gene expression at each spot as a mixture of cell types. We first generated a reference scRNA-seq object using high-confidence cell-type annotations from our single-cell dataset. This reference was formatted using the Reference class in SpaceXr, which aggregates gene expression profiles and cell-type labels. Spatial transcriptomics data were preprocessed using standard normalization and log-transformation. We then constructed a SpatialRNA object for the spatial data and ran the create. RCTD function to initialize the model. The deconvolution was performed using the run. RCTD function with doublet mode enabled to allow for mixed-cell-type predictions per spot. These proportions were visualized across tissue sections to assess spatial distribution and interactions. Spatial colocalization of key cell types (e.g., CETP$^+$ macrophages, APOA2$^+$ tumor cells, IT_T cells) was further analyzed using spatial correlation metrics and proximity-based enrichment.

Supplementary Information

The online version contains supplementary material available at https://doi.org/10.1186/s12964-026-02689-3.

Supplementary Material 1.

Acknowledgements

We deeply thank all the contribution of the involved patients in this study. The sequencing was provided by OE Biotech Co., Ltd. (Shanghai, China).

Code availability
The custom code used in this study is not publicly available but can be obtained from the corresponding author upon reasonable request.

Authors' contributions
Yizhi Ge and Haitao Liu contributed to the conceptualization, design, writing, methodology, and analyses of this study. Jiayi Shen and Hongming Xu participated in patients' selection, clinical information and sample collection. Yong Feng, Dan Zong, and Lijun Wang performed conceptualization, design, data analysis and critically revised the manuscript. All authors approved the final version and agreed to be accountable for all aspects of the work.

Funding
We appreciate the fund support by Wu Jieping Medical Foundation [No. 320.6750.2024-13-50], New Frontier Research Project for Tumor Supportive Treatment [No. cphcf-2023-255].

Data availability
The datasets generated and analyzed during the current study are not publicly available due to patient privacy and institutional regulations but are available from the corresponding author on reasonable request.

Declarations

Ethics approval and consent to participate
This research was approved by the Research Ethics Committee of Jiangsu Cancer Hospital [No.2023-046]. All patients have written informed consent for participation in this study.

Competing interests
The authors declare no competing interests.

Received: 14 August 2025 / Accepted: 19 January 2026
Published online: 07 February 2026

References

1. Eng C, et al. Colorectal cancer. Lancet. 2024;404:294–310.
2. Bertocchi A, et al. Gut vascular barrier impairment leads to intestinal bacteria dissemination and colorectal cancer metastasis to liver. Cancer Cell. 2021;39:708–24.
3. Li J, et al. Remodeling of the immune and stromal cell compartment by PD-1 Blockade in mismatch repair-deficient colorectal cancer. Cancer Cell. 2023;41:1152–69.
4. Tauriello D, et al. TGFbeta drives immune evasion in genetically reconstituted colon cancer metastasis. Nature. 2018;554:538–43.
5. Saberzadeh-Ardestani B, et al. Metastatic site and clinical outcome of patients with deficient mismatch repair metastatic colorectal cancer treated with an immune checkpoint inhibitor in the first-line setting. Eur J Cancer. 2024;196:113433.
6. Galluzzi L, Aryankalayil MJ, Coleman CN, Formenti SC. Emerging evidence for adapting radiotherapy to immunotherapy. Nat Rev Clin Oncol. 2023;20:543–57.
7. Sakai SA, et al. Single-cell Spatial analysis with xenium reveals anti-tumour responses of CXCL13 + T and CXCL9 + cells after radiotherapy combined with anti-PD-L1 therapy. Br J Cancer. 2025;133:795–808.
8. Lind HT, et al. MHC class I upregulation contributes to the therapeutic response to radiotherapy in combination with anti-PD-L1/anti-TGF-beta in squamous cell carcinomas with enhanced CD8 T cell memory-driven response. Cancer Lett. 2025;608:217347.
9. Ding Y, et al. High and low dose radiotherapy combined with ICIs for MSS colorectal cancer patients with liver metastases: a phase I study (HaRyPOT). Front Oncol. 2025;15:1503517.
10. Bian X et al. Lipid metabolism and cancer. J Exp Med 218. 2021.
11. Lim SA, Su W, Chapman NM, Chi H. Lipid metabolism in T cell signaling and function. Nat Chem Biol. 2022;18:470–81.
12. Yan J, Horng T. Lipid metabolism in regulation of macrophage functions. Trends Cell Biol. 2020;30:979–89.
13. Lee CH, Plutzky J. Liver X receptor activation and high-density lipoprotein biology: a reversal of fortune? Circulation. 2006;113:5–8.
14. Das S, et al. Liver X receptor unlinks intestinal regeneration and tumorigenesis. Nature. 2025;637:1198–206.
15. Lou X, et al. Structure of the retinoid X receptor alpha-liver X receptor beta (RXRalpha-LXRbeta) heterodimer on DNA. Nat Struct Mol Biol. 2014;21:277–81.
16. Luo Y, Liang CP, Tall AR. The orphan nuclear receptor LRH-1 potentiates the sterol-mediated induction of the human CETP gene by liver X receptor. J Biol Chem. 2001;276:24767–73.
17. Sanjurjo L, Aran G, Roher N, Valledor AF, Sarrias MR. AIM/CD5L: a key protein in the control of immune homeostasis and inflammatory disease. J Leukoc Biol. 2015;98:173–84.
18. Kowal K, et al. CD163 and its role in inflammation. Folia Histochem Cytobiol. 2011;49:365–74.
19. Chow A, et al. Tim-4(+) cavity-resident macrophages impair anti-tumor CD8(+) T cell immunity. Cancer Cell. 2021;39:973–88.
20. Zhang Z, et al. Cancer-associated fibroblasts-derived CXCL12 enhances immune escape of bladder cancer through inhibiting P62-mediated autophagic degradation of PDL1. J Exp Clin Cancer Res. 2023;42:316.
21. Huang L, et al. Mrc1(+) macrophage-derived IGF1 mitigates crystal nephropathy by promoting renal tubule cell proliferation via the AKT/Rb signaling pathway. Theranostics. 2024;14:1764–80.
22. Hao Y, et al. Dictionary learning for integrative, multimodal and scalable single-cell analysis. Nat Biotechnol. 2024;42:293–304.
23. Tang Z, Kang B, Li C, Chen T, Zhang Z. GEPIA2: an enhanced web server for large-scale expression profiling and interactive analysis. Nucleic Acids Res. 2019;47:W556–60.
24. Korsunsky I, et al. Fast, sensitive and accurate integration of single-cell data with harmony. Nat Methods. 2019;16:1289–96.
25. Patel AP, et al. Single-cell RNA-seq highlights intratumoral heterogeneity in primary glioblastoma. Science. 2014;344:1396–401.
26. Cao J, et al. The single-cell transcriptional landscape of mammalian organogenesis. Nature. 2019;566:496–502.
27. Aibar S, et al. SCENIC: single-cell regulatory network inference and clustering. Nat Methods. 2017;14:1083–6.
28. Jin S, Plikus MV, Nie Q. CellChat for systematic analysis of cell-cell communication from single-cell transcriptomics. Nat Protoc. 2025;20:180–219.
29. Browaeys R, Saelens W, Saeys Y. NicheNet: modeling intercellular communication by linking ligands to target genes. Nat Methods. 2020;17:159–62.
30. Cable DM, et al. Robust decomposition of cell type mixtures in Spatial transcriptomics. Nat Biotechnol. 2022;40:517–26.
31. McLaughlin M, et al. Inflammatory microenvironment remodelling by tumour cells after radiotherapy. Nat Rev Cancer. 2020;20:203–17.
32. Ismail OZ, Bhayana V. Lipase or amylase for the diagnosis of acute pancreatitis? Clin Biochem. 2017;50:1275–80.
33. Liu C, et al. Single-cell RNA-sequencing reveals radiochemotherapy-induced innate immune activation and MHC-II upregulation in cervical cancer. Signal Transduct Target Ther. 2023;8:44.
34. Nielsen MC et al. Macrophage Activation Markers, CD163 and CD206, in Acute-on-Chronic Liver Failure. *Cells*. 9. 2020.
35. Ko CY, et al. Omentin-1 ameliorates the progress of osteoarthritis by promoting IL-4-dependent anti-inflammatory responses and M2 macrophage polarization. Int J Biol Sci. 2023;19:5275–89.
36. Sarkar S, et al. APOA2 increases cholesterol efflux capacity to plasma HDL by displacing the C-terminus of resident APOA1. J Lipid Res. 2024;65:100686.
37. Reinfeld BI, et al. Cell-programmed nutrient partitioning in the tumour microenvironment. Nature. 2021;593:282–8.
38. Waddington KE, Jury EC. Pineda-Torra, I. Liver X receptors in immune cell function in humans. Biochem Soc Trans. 2015;43:752–7.
39. Blauw LL, Wang Y, Willems VDK, Rensen P. A novel role for CETP as immunological gatekeeper: Raising HDL to cure sepsis? Trends Endocrinol Metab. 2020;31:334–43.
40. Zeljkovic A et al. Revealing the role of High-Density lipoprotein in colorectal cancer. Int J Mol Sci 22. 2021.
41. Sanjurjo L, et al. CD5L promotes M2 macrophage polarization through Autophagy-Mediated upregulation of ID3. Front Immunol. 2018;9:480.
42. K. M. Turner. Extrachromosomal oncogene amplification drives tumour evolution and genetic heterogeneity. Nature. 2017;543:122–5.

Publisher's Note